

Slip-dominated structural transitions

Kanka Ghosh,^{1,*} Oguz Umut Salman,¹ Sylvain Queyreau,¹ and Lev Truskinovsky^{2,†}

¹CNRS, LSPM UPR 3407, Université Sorbonne Paris Nord, 93430 Villetaneuse, France

²PMMH, CNRS UMR 7636 ESPCI ParisTech, 10 Rue Vauquelin, 75005 Paris, France

We use molecular dynamics to show that plastic slip is a crucial component of the transformation mechanism of a square-to-triangular structural transition. The latter is a stylized analog of many other reconstructive phase transitions. To justify our conclusions we use a novel atomistically-informed mesoscopic representation of the field of lattice distortions in molecular dynamics simulations. Our approach reveals a hidden alternating slip distribution behind the seemingly homogeneous product phase which points to the fact that lattice invariant shears play a central role in this class of phase transformations. While the underlying pattern of anti-parallel displacements may be also interpreted as microscopic shuffling, its precise crystallographic nature strongly suggests the plasticity-centered interpretation.

Reconstructive phase transitions are the most widespread type of structural transformations in solids. These transitions lack the simplifying group-subgroup relationship and therefore cannot be described by the conventional Landau theory. The development of the equally encompassing theory of reconstructive transitions is still a challenge given that they involve breaking of chemical bonds and are characterized by micro-inhomogeneous configurations with slip, twinning, and stacking faults apparently intertwined [1–7].

The BCC-HCP reconstructive transition is one of the most representative [8–15]. Its mechanism, proposed by Burgers based on crystallographic analysis [16–23], implies the presence of a homogeneous shear and a superimposed alternating shuffling represented by anti-parallel shifting of atomic layers. The origin of the shuffling cannot be addressed based on crystallography only and various attempts to interpret it while referring to structural mechanics, energetics and kinetics can be found in the literature [14, 17, 24–32]. Similar problem exists for the FCC-HCP reconstructive phase transition which can be accomplished crystallographically by the alternating coordinated gliding of Shockley partials on every second close-packed crystallographic plane [33, 34]. The origin of the implied antagonistic displacements still remain obscure despite many insightful attempts to link it to first principles auxiliary computations [33, 35–49].

More generally, the pattern of anti-parallel, crystallographically specific, nanoscale, highly coordinated displacements appear to be a distinguishing feature of reconstructive transitions, which is the main factor placing them outside the classical Landau picture [1, 50, 51]. A fundamental understanding of this phenomenon is then of great theoretical interest and in this Letter we propose its new interpretation. Our conclusions are based on systematic molecular dynamics (MD) studies of a prototypical model which suggest that the crucial *non-Landau* factor in reconstructive phase transitions is the disguised plastic slip.

Specifically, we study the simplest reconstructive transition between 2D square (S) and triangular (T) lat-

tices [2, 52, 53]. While such square-to-hexagonal phase change is of interest by itself [54–68], it can be considered as a stylized, low dimensional, Bravais lattice analog of both emblematic BCC-HCP and FCC-HCP reconstructive transitions [69–71].

To interpret the results of our MD simulations we shift attention from the conventional focus on the configurations of *individual* atoms to the original representation of the transformation history in terms of the evolution of atomic *neighborhoods*. This new approach allows us to map the transformation path into the configurational space of the mesoscopic metric tensors. The purely geometrical periodic tessellation of the latter creates the possibility to distinguish unambiguously between elastic and plastic deformations [2, 53, 72]. The application of such atomistically-informed representation of lattice distortions in the case of S-T transition reveals that its fundamentally non-affine mechanism involves alternating lattice invariant shears which points towards a plasticity-centered interpretation of this reconstructive transition. To corroborate the results of our MD experiments, we also performed a parallel study of a coarse grained mesoscopic model which directly deals with the evolution of atomic neighborhoods [72–76]. The obtained qualitative agreement suggests that the observed slip-dominated mechanism of S-T transition is a robust feature of this class of reconstructive transformations, insensitive to microscopic details.

The molecular dynamics simulations were carried out using LAMMPS [77, 78]. The particle interaction potential was chosen in the form $V(r) = a/r^{12} - c_1 \exp[-b_1(r - r_1)^2] - c_2 \exp[-b_2(r - r_2)^2]$, allowing one to stabilize in 2D both square and triangular lattices [79]; here r_1 is the lattice constant and r_2 is the second nearest neighbor distance. Periodic boundary conditions were employed and pressure controlled protocol was implemented within isothermal-isobaric ensemble [80]. The computed (kinetic) T-P phase diagram for the direct S-T transition is shown in Fig. 1(a). The predicted negative slope of the coexistence curve agrees with similar numerical experiments [81–83] and is also

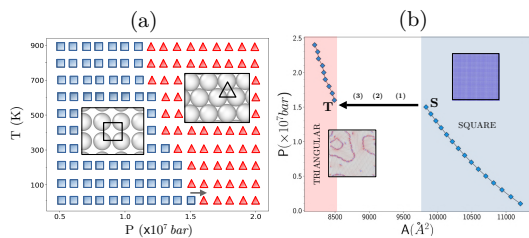


FIG. 1. MD simulated square-to-triangular transition: (a) kinetic T-P phase diagram showing only the direct transition; (b) the same transition in P-V (area A) performed at $T = 10$ K (as indicated in (a) by an arrow).

consistent with the data for BCC-HCP transformation in iron [84, 85]. In Fig. 2 we illustrate the fact that the originally pure-crystalline square lattice transforms into a poly-crystalline triangular configuration with specifically mis-oriented grains separated by dislocation-rich curved grain boundaries [80].

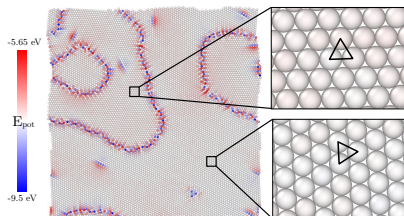


FIG. 2. Multigrain configuration of transformed triangular lattice (T) colored according to the potential energy of each atom. The atomic structure of two triangular grains with 30° mis-orientation is illustrated in the insets.

As a novel way of interpreting the results of MD simulations, we extracted from individual atomic position data the local values of the deformation gradients. This amounts to post-processing the instantaneous MD data which are then interpreted as representing piecewise linear strain fields [86–90]. Specifically, by denoting the reference discrete atomic positions \mathbf{x}^i and the deformed atomic positions \mathbf{y}^i , we can define the effective deformation gradient \mathbf{F}^i by minimizing the error function $\sum \|\Delta\mathbf{y} - \mathbf{F}^i \Delta\mathbf{x}\|^2$ with summation over the pairs of elements inside the chosen neighborhood of a given site i [91–97]. In our case of weakly distorted lattices the sampling neighborhood could be limited to two complementary triangular domains [80]. Most importantly, this approach allows us to compute the MD informed local metric tensor $\mathbf{C}^i = \mathbf{F}^{iT} \mathbf{F}^i$.

The possibility of mapping the results of MD simulations into the \mathbf{C} -space (with coordinates C_{11} , C_{22} , and C_{12}) is of great interest because its crucial subspace, $\det(\mathbf{C}) = 1$, is naturally tessellated by the action of the global symmetry group of Bravais lattices. The latter is a finite strain extension of the crystallographic

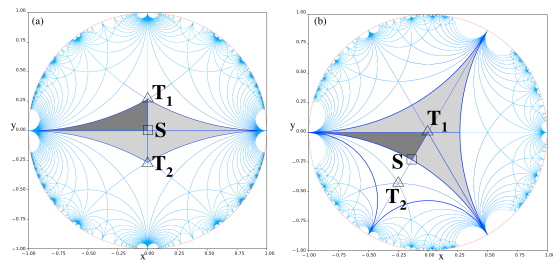


FIG. 3. Stereographic projection on a Poincaré disk of the configurational space of metric tensors \mathbf{C} with $\det \mathbf{C} = 1$ given by the formulas $x = t(C_{11} - C_{22})/2$, $y = tC_{12}$, where $t = 2(2 + C_{11} + C_{22})^{-1}$, see [80] for details. In (a,b) the reference states are the square phase S and the triangular phase T_1 , respectively. Dark gray indicates the minimal periodicity domain, light gray – the minimal elastic domain; blue lines represent the tessellation induced by the $GL(2, \mathbb{Z})$ global symmetry.

point group and can be represented in our case explicitly: $GL(2, \mathbb{Z}) = \{\mathbf{m}, m_{IJ} \in \mathbb{Z}, \det(\mathbf{m}) = \pm 1\}$, see for instance [2, 53, 98–112].

The symmetry-induced periodicity structure in the space of metric tensors \mathbf{C} is illustrated in Fig. 3(a,b), where we identify both, the minimal periodicity (fundamental) domain and the minimal *elastic domain* (fundamental domain extended under the action of the point group), see [80] and also [75, 76] for more details. The two panels in Fig. 3 provide equivalent information with the only difference that in (a) the \mathbf{C} -space is centered around the reference square lattice (point S), while in (b) the reference lattice is triangular (point T_1) [80]. The importance of Fig. 3(b) for what follows is that it clearly indicates that the two triangular lattices T_1 and T_2 belong to different *elastic domains* because they differ by a lattice invariant shear representing an elementary plastic slip.

In Fig. 4(a) we show in more detail a fragment of the \mathbf{C} -space centered around the point S (taken in this case as the reference, essentially a zoom in on Fig. 3(a)). One can see that an unbiased (pressure or temperature induced) S-T transition would be represented in Fig. 4(a) simultaneously by *two* paths: $S \rightarrow T_1$ and $S \rightarrow T_2$. Both paths describe pure shear deformations traversing configurations with rhombic symmetry; while those are isochoric projections, the actual MD transition is also accompanied by a volumetric contraction, see [80]. If we advance from \mathbf{C} -space to the larger \mathbf{F} -space, even more complex picture emerges, see Fig. 4(b). Thus, the “deformation variants” in \mathbf{C} -space multiply as “orientation variants” in \mathbf{F} -space where the same deformation can correspond to several different orientations of the basis vectors.

More specifically, observe first that the stretch tensor $\mathbf{U}_\diamond(\lambda) = \sqrt{\mathbf{C}_\diamond}$ along the path $S \rightarrow T_1$ can be written in

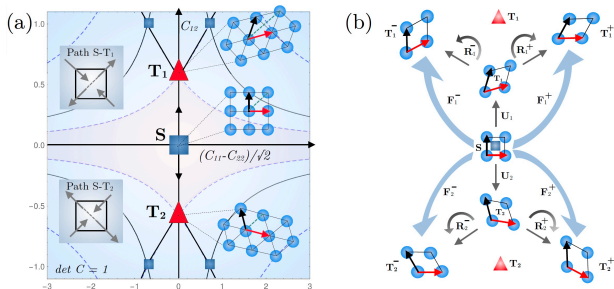


FIG. 4. (a) A fragment of the configurational space of metric tensors \mathbf{C} showing the original square lattice (point S) and two equivalent versions of the triangular lattice (points T_1 and T_2). Solid arrows are directed along the two symmetric pure shear (rhombic) paths $S \rightarrow T_1$ and $S \rightarrow T_2$; the *elastic domain* is shown in pink; (b) A schematic structure of the four equivalent transformation paths in the extended configurational space of metric tensors \mathbf{F} emphasizing rotations needed to recover the geometric compatibility with the square phase.

the form [113]

$$\mathbf{U}_\diamond(\lambda) = \frac{1}{2} \begin{bmatrix} \lambda + \frac{1}{\lambda} & \lambda - \frac{1}{\lambda} \\ \lambda - \frac{1}{\lambda} & \lambda + \frac{1}{\lambda} \end{bmatrix}, \quad (1)$$

where $\lambda = 1$ at the square phase S and $\lambda = \lambda_* = 3^{1/4}$ at the triangular phase T_1 ; along the synchronous path $S \rightarrow T_2$ the stretch tensor is $\mathbf{U}_\diamond(1/\lambda)$. Note next, that the mappings $\mathbf{U}_1 = \mathbf{U}_\diamond(\lambda_*)$ and $\mathbf{U}_2 = \mathbf{U}_\diamond(\lambda_*^{-1})$, describe area preserving stretching along two opposite diagonals of a square lattice cell with one of the diagonals becoming longer than the other. These mappings, however, do not fully characterize the complete $S \rightarrow T$ transition because the underlying rigid rotation remains unspecified. For instance, to ensure geometrically compatible lattice orientations, a clockwise rotation $\mathbf{R}^+(\vartheta)$ and anti clockwise rotation $\mathbf{R}^-(\vartheta)$ with $\vartheta = \pm 15^\circ$ have to be added to \mathbf{U}_1 and \mathbf{U}_2 . Such specification of rotations produces four equivalent triangular lattices T_1^+ , T_1^- , T_2^+ and T_2^- shown schematically in Fig. 4(b). The corresponding deformation gradients are $\mathbf{F}_{1,2}^\pm = \mathbf{R}_{1,2}^\pm \mathbf{U}_{1,2}$, where, for instance,

$$\mathbf{R}_1^+ = \frac{1}{\sqrt{\cosh \alpha}} \begin{bmatrix} \cosh(\alpha/2) & \sinh(\alpha/2) \\ -\sinh(\alpha/2) & \cosh(\alpha/2) \end{bmatrix}, \quad (2)$$

with $\alpha = 2 \ln \lambda_*$: the rotation aligns in this case the basis vector \mathbf{e}_1 (already rotated by the mapping $\mathbf{U}_\diamond(\lambda_*)$) with the horizontal direction.

In Fig. 5(a,d) we show that all four variants $T_{1,2}^\pm$ have been indeed observed in our MD experiments. One can see that the two representations of the same atomic configuration, reached at the end of the S-T transformation, feature alternating rows/columns of positive and negative components of the deformation gradients, F_{12}^\pm and F_{21}^\pm , see Fig. 5(b,e). In other words, we observe mixtures of alternating states, either T_1^+ and T_2^- , in Fig.

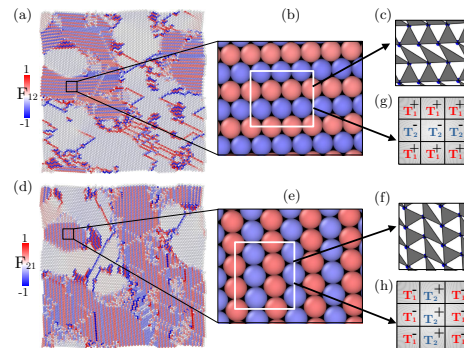


FIG. 5. In (a), (d) we depict the MD simulated fields F_{12} and F_{21} in the transformed triangular phase. Zoomed-in views of fragments from (a,d) are presented in (b,e) where we see the corresponding atomic configurations visualized using OVITO [114]. In (c,f) we show triangulation representations corresponding to zoomed-in fragments from (b,e). In (g,h) we identify the corresponding variants $T_{1,2}^\pm$.

5(g), or T_1^- and T_2^+ , in Fig. 5(h). In Fig. 5(c,f) we illustrate the associated Delaunay triangulations visualizing the non-affine deformation behind the apparently homogeneous grains. The parallel numerical experiments using athermal molecular statics fully corroborate these rather remarkable observations, see [80] for details.

The main conclusion is that the standard representation of MD data, showing in the case of the S-T transition a polycrystal with mis-oriented homogeneous grains, is deceptive. Instead, our new way of representing MD data reveals crystallographically specific nano-twinning disguised as rigid rotations. Given that the underlying antiparallel atomic displacements correspond *exactly* to lattice invariant shears, it is natural to interpret the resulting pattern as representing alternating plastic slips. The emerging depiction of the transformation path complements and broadens previous studies of the mechanism of the S-T transition [1, 2, 18, 51, 53, 62, 81, 83, 115–120]. The apparently overlooked peculiarity of the S-T transition is the possibility to compose elementary variants of the product phase at the atomic level to obtain the final configuration with no overall shear deformation and no ‘surface’ energy penalty inside any of the grains.

Additional insights can be obtained if we present the obtained strain distribution against the energy landscape $\phi(\mathbf{C})$ in the \mathbf{C} -space. To construct such a landscape it is sufficient to apply homogeneous deformation \mathbf{C} to a mesoscopic set of atoms, while accounting for all pairwise interactions, and then use the Cauchy-Born rule [121, 122] and write $\phi(\mathbf{C}) = \frac{1}{2\Omega} \sum_{\mathbf{x}} \sum_{\mathbf{x}^c \in \mathcal{N}(\mathbf{x})} V(\sqrt{R_i C_{ij} R_j})$, where R_i are the vectors representing reference points and the internal summations extend over all points \mathbf{x}^c belonging to the cut-off neighborhood $\mathcal{N}(\mathbf{x})$. The globally symmetric potential $\phi(\mathbf{C})$ emerges if we extend by $GL(2, \mathbb{Z})$ periodicity the results of computations

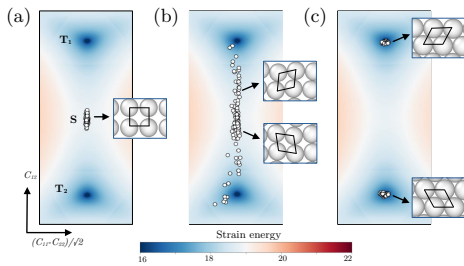


FIG. 6. Gradual progression of the S→T transformation in \mathbf{C} -space at three different stages corresponding to points (1-3) indicated in Fig. 1(b). Fragments of the initial square and the transformed rhombic and triangular configurations are shown in the insets. The energy landscape is visible at the background.

performed in a single *elastic domain*.

In Fig. 6, we show a fragment of the computed energy landscape around the reference configuration S which includes the two target configurations T_1 and T_2 . We mapped into the same \mathbf{C} -space the atomic strains from our MD simulations while showing separately the three stages (1-3) of the S-T transition indicated in Fig. 1(b). Specifically, Fig. 6(a) shows the beginning of the transformation when all atomic strains populate the marginally stable square configuration S located at the origin. At the intermediate stage of the transformation, shown in Fig. 6(b), we observe spreading of atomic strains along the two symmetric rhombic (pure shear) paths towards two energy wells representing the variants T_1 and T_2 . Note that both paths are pursued simultaneously and, as a result, the transformed triangular phase emerges as comprised of strains populating both energy wells T_1 and T_2 , see Fig. 6(c). A broader picture, representing also a small number of elements which end up in distant energy wells, can be found in [80].

Further analysis of the stage-by-stage transformation process in the physical space, see Fig. 7(a), shows that the alternating micro-slips (represented by oscillatory fields F_{12} or F_{21}) develop layer-by-layer through back and forth transverse propagation of Shockley partials; the possibility of such nano-scale ‘zipping’ by moving surface steps is well known, see for instance [123]. At larger scale the transformation will appear as proceeding through front propagation which leaves behind a pattern of anti-parallel displacements disguised as a rigid rotation of a perfect triangular lattice, see Fig. 7(b-e).

Using the constructed multi-well periodic potential $\phi(\mathbf{C})$ we can now develop a coarse grained description of the system. The simplest way to obtain a regularized theory is to assume that such potential describes mechanical response of elastic finite elements whose size introduces a mesoscopic cut-off spatial scale [72, 73, 75, 121]. The piece-wise affine deformation of the elements can be then presented in the form $\mathbf{y}(\mathbf{x}) = \mathbf{y}_{ij}N_{ij}(\mathbf{x})$, where \mathbf{y}_{ij}

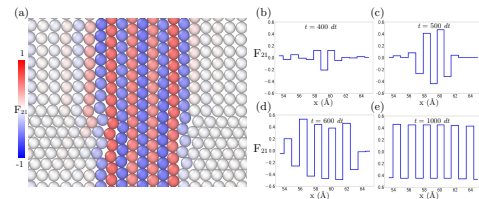


FIG. 7. (a) Layer-by-layer propagation of the deformation gradient (here only F_{21} component) during S-T transformation; (b-e) transient spatial configurations of the deformation gradient showing the formation of an ideally periodic pattern.

is the deformation of the 2D network of discrete nodes and $N_{ij}(\mathbf{x})$ are the linear shape functions. The problem reduces to finite dimensional parametric minimization of the energy functional $W = \int_{\Omega_0} \phi(\mathbf{C})d\Omega_0$, where Ω_0 is the computational domain, see [80] for details. The outcome of such mesoscopic modeling of the S-T transformation process is illustrated in Fig. 8. As in our molecular simulations we started with a perfect square lattice brought to a marginally stable state. In the emerging polycrystalline configuration, see Fig. 2, we again observe a texture of triangular grains with mis-orientation of 30° . The boundaries of the grains are similarly dislocation-rich even if now the dislocation cores are blurred at the cut-off scale of elastic finite elements. The transformation is again advancing along two concurrent rhombic (pure shear) paths with eventual lock-in on the higher symmetry configurations T_1 and T_2 [80]. In the final configuration, the apparent rotations are again achieved through alternating crystallographically specific slips inside the adjacent planes with the formation of the same two types of variant mixtures (T_1^+, T_2^-) and (T_1^-, T_2^+), see Fig. 8.

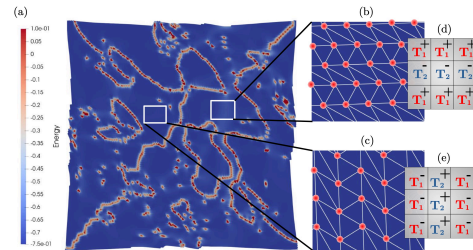


FIG. 8. Outcome of the coarse grained modeling of S-T transition: (a) The post-transformation polycrystalline texture; (b-c) two fragments of mis-oriented triangular grains, with (b) presenting (T_1^+, T_2^-) variant mixture and (c) representing (T_1^-, T_2^+) variant mixture.

We can now try to draw some parallels between the observed mechanism of the S-T transition in 2D and, for instance, the mechanism of the reconstructive BCC-HCP transition in 3D [85, 124]. While the latter involves volume preserving pure shear deformation in addition to shuffling, those two phenomena appear to be well separated in time and therefore can be decoupled [125]. We

can then, following [18], neglect the Landau-type component of the transformation by associating the primary order parameter with the shuffle. Note that a shuffle would have naturally emerged in S-T transition if in our reconstruction of atomistic deformation gradients we had used a double unit cell [126]. Usually the BCC-HCP shuffle is perceived as proceeding via softening of an optical mode with the formation of an intermediate orthorhombic configuration with an idea that such lowering of symmetry is maintained until the system locks-in in the higher symmetry configuration [127]. Our analysis suggests that it can be viewed, in the first approximation, as a pattern of anti-parallel shifts of consecutive planes inside a single unit-cell (probably with some homogeneous adjustment layer-wise). The large transformation strain in the lock-in conditions drives the scale of such apparent micro-twinning to atomic dimensions.

The proposed analogy should be viewed with caution as the BCC-HCP transition in 3D is still different from the S-T transition in 2D. Thus, it is not clear whether the experimentally confirmed path for BCC-HCP transition [17] can be decomposed into full plastic slips or instead represented by alternating stacking faults resulting from the passage of only partial dislocations. Thus, the reconstructive FCC-HCP transition appear to be an example of the latter possibility as in this case the HCP phase emerges from an anti-parallel coordinated gliding of Shockley partials [38–40, 128, 129]. In the setting of S-T transformation the implied nano-scale stacking fault laminate [33, 48] would correspond to the layering of the type T_1 - S - T_2 . Since in our case the S phase is unstable, such ‘partially’ plastic laminates are not observed with partials appearing only transiently as it is clear from our Fig. 7(a).

To conclude, we showed that tracking the history of atomic-scale metric tensors in MD simulations offers a unique perspective on the intricate micro-pattern formation during reconstructive phase transitions. The proposed interpretation of MD numerical experiments reveals previously hidden details of the deformation paths allowing one to analyze systematically the underlying relation between elastic and inelastic modes. The micro-mechanism, shown to be operative during the prototypical S-T transition, contains some generic elements which are expected to be common for most reconstructive transitions including the iconic BCC-HCP and FCC-HCP transitions.

Acknowledgments. The authors are grateful to D. Gratias, C. Denoual and Y.P. Pellegrini for helpful suggestions in the course of this work. K.G and O.U.S. were supported by Grant ANR-19-CE08-0010. L.T. acknowledges the support of the Grants ANR-17-CE08-0047-02, ANR-21-CE08-MESOCRYSP and ERC-H2020-MSCA-RISE-2020-101008140.

-
- * kanka.ghosh@lspm.cnrs.fr
 † lev.truskinovsky@espci.fr
- [1] P. Tolédano and V. Dmitriev, *Reconstructive Phase Transitions* (WORLD SCIENTIFIC, 1996) <https://www.worldscientific.com/doi/pdf/10.1142/2848>.
 - [2] K. Bhattacharya, S. Conti, G. Zanzotto, and J. Zimmer, *Nature* **428**, 55 (2004).
 - [3] J. W. Cahn, *Acta Metallurgica* **25**, 721 (1977).
 - [4] Y. Gao, R. Shi, J.-F. Nie, S. A. Dregia, and Y. Wang, *Acta Materialia* **109**, 353 (2016).
 - [5] Y. Gao, S. A. Dregia, and Y. Wang, *Acta Materialia* **127**, 438 (2017).
 - [6] K. Otsuka and X. Ren, *Progress in materials science* **50**, 511 (2005).
 - [7] B. Li, D. Zhou, and Y. Han, *Nature Reviews Materials* **1**, 1 (2016).
 - [8] D. Bancroft, E. L. Peterson, and S. Minshall, *Journal of Applied Physics* **27**, 291 (1956).
 - [9] K. J. Caspersen, A. Lew, M. Ortiz, and E. A. Carter, *Physical Review letters* **93**, 115501 (2004).
 - [10] D. Kalantar, J. Belak, G. Collins, J. Colvin, H. Davies, J. Eggert, T. Germann, J. Hawreliak, B. Holian, K. Kadau, *et al.*, *Physical Review Letters* **95**, 075502 (2005).
 - [11] C. Baruffi, A. Finel, Y. Le Bouar, B. Bacroix, and O. U. Salman, *Computational Materials Science* **203**, 111057 (2022).
 - [12] D. A. Young, *Phase diagrams of the elements* (Univ of California Press, 1991).
 - [13] S. Banerjee and P. Mukhopadhyay, *Phase transformations: examples from titanium and zirconium alloys* (Elsevier, 2010).
 - [14] H. Zong, P. He, X. Ding, and G. J. Ackland, *Physical Review B* **101**, 144105 (2020).
 - [15] G. Grimvall, B. Magyari-Köpe, V. Ozoliņš, and K. A. Persson, *Reviews of Modern Physics* **84**, 945 (2012).
 - [16] W. Burgers, *Physica* **1**, 561 (1934).
 - [17] H.-K. Mao, W. A. Bassett, and T. Takahashi, *Journal of Applied Physics* **38**, 272 (1967).
 - [18] S. Srinivasan, D. Hatch, H. Stokes, A. Saxena, R. Albers, and T. Lookman, *arXiv preprint cond-mat/0209530* (2002).
 - [19] W. Bassett and E. Huang, *Science* **238**, 780 (1987).
 - [20] S. Wang, M. Sui, Y. Chen, Q. Lu, E. Ma, X. Pei, Q. Li, and H. Hu, *Scientific reports* **3**, 1086 (2013).
 - [21] K. Masuda-Jindo, S. Nishitani, and V. Van Hung, *Physical Review B* **70**, 184122 (2004).
 - [22] S. Merkel, A. Lincot, and S. Petitgirard, *Physical Review B* **102**, 104103 (2020).
 - [23] T.-H. Lee, H.-Y. Ha, J.-Y. Kang, J. Moon, C.-H. Lee, and S.-J. Park, *Acta materialia* **61**, 7399 (2013).
 - [24] D. Banerjee, K. Muraleedharan, and J. Strudel, *Philosophical Magazine A* **77**, 299 (1998).
 - [25] J. Zhao, D. Maroudas, and F. Milstein, *Physical Review B* **62**, 13799 (2000).
 - [26] C. Cayron, *Acta Materialia* **111**, 417 (2016).
 - [27] C. Cayron, F. Barcelo, and Y. de Carlan, *Acta materialia* **58**, 1395 (2010).
 - [28] S. Van Bohemen, J. Sietsma, and S. Van der Zwaag, *Physical Review B* **74**, 134114 (2006).
 - [29] A. H. Zahiri, J. Ombogo, M. Lotfipour, and L. Cao, *Met-*

- als **13**, 525 (2023).
- [30] M. Sanati, A. Saxena, T. Lookman, and R. Albers, *Physical Review B* **63**, 224114 (2001).
- [31] J. Liu and D. D. Johnson, *Physical Review B* **79**, 134113 (2009).
- [32] V. Riffet, B. Amadon, N. Bruzy, and C. Denoual, *Physical Review Materials* **4**, 063609 (2020).
- [33] Y. M. Jin, A. G. Khachatryan, Y. U. Wang, C. R. Krenn, and A. J. Schwartz, *Metallurgical and Materials Transactions A* **36**, 2031 (2005).
- [34] G. B. Olson and M. Cohen, *Metallurgical Transactions A* **7**, 1897 (1976).
- [35] E. Gartstein and A. Rabinkin, *Acta Metallurgica* **27**, 1053 (1979).
- [36] H. Fujita and S. Ueda, *Acta Metallurgica* **20**, 759 (1972).
- [37] T. Waitz and H. Karnthaler, *Acta materialia* **45**, 837 (1997).
- [38] Y. Liu, H. Yang, G. Tan, S. Miyazaki, B. Jiang, and Y. Liu, *Journal of alloys and compounds* **368**, 157 (2004).
- [39] H. Yang and Y. Liu, *Acta materialia* **54**, 4895 (2006).
- [40] Y. Liu, H. Yang, Y. Liu, B. Jiang, J. Ding, and R. Woodward, *Acta materialia* **53**, 3625 (2005).
- [41] B. Li, G. Qian, A. R. Oganov, S. E. Boulfelfel, and R. Faller, *The Journal of Chemical Physics* **146** (2017).
- [42] H. Zhang, B. Wei, X. Ou, S. Ni, H. Yan, and M. Song, *International Journal of Plasticity* **156**, 103357 (2022).
- [43] W. Guo, F. Han, G. Li, Y. Zhang, M. Ali, J. Ren, Q. Wang, and F. Yuan, *Journal of Materials Science & Technology* **137**, 8 (2023).
- [44] S. Li, P. J. Withers, W. Chen, and K. Yan, *Journal of Materials Science & Technology* **210**, 138 (2025).
- [45] F. Zhang, Y. Ren, Z. Pei, Q. Gao, Z. Lu, B. Wang, Y. Xue, X. Cao, K. Du, Y. Yang, *et al.*, *Acta Materialia* **276**, 120150 (2024).
- [46] E. Farabi, N. Haghdadi, C. Czettel, J. Pachlhofer, G. Rohrer, S. Ringer, and S. Primig, *Scripta Materialia* **248**, 116127 (2024).
- [47] R. Fréville, A. Dewaele, N. Bruzy, V. Svitlyk, and G. Garbarino, *Physical Review B* **107**, 104105 (2023).
- [48] A. Rosa, A. Dewaele, G. Garbarino, V. Svitlyk, G. Morard, F. De Angelis, M. Krstulović, R. Briggs, T. Irifune, O. Mathon, *et al.*, *Physical Review B* **105**, 144103 (2022).
- [49] E. Galindo-Nava, *Materialia* **33**, 102033 (2024).
- [50] V. Dmitriev, S. Rochal, Y. M. Gufan, and P. Toledano, *Physical Review letters* **60**, 1958 (1988).
- [51] V. Dmitriev, *Discontinuous Phase Transitions in Condensed Matter: Symmetry Breaking in Bulk Martensite, Quasiperiodic and Low-Dimensional Nanostructures* (World Scientific, 2023).
- [52] E. Arbib, P. Biscari, C. Patriarca, and G. Zanzotto, *Journal of Elasticity* **155**, 747 (2024).
- [53] S. Conti and G. Zanzotto, *Archive for rational mechanics and analysis* **173**, 69 (2004).
- [54] J. M. e Silva and B. Mokross, *Physical Review B* **21**, 2972 (1980).
- [55] M. Eskildsen, P. Gammel, B. Barber, U. Yaron, A. Ramirez, D. Huse, D. Bishop, C. Bolle, C. Lieber, S. Oxx, *et al.*, *Physical Review letters* **78**, 1968 (1997).
- [56] B. Keimer, W. Y. Shih, R. W. Erwin, J. W. Lynn, F. Dogan, and I. A. Aksay, *Physical Review letters* **73**, 3459 (1994).
- [57] D. Chang, C.-Y. Mou, B. Rosenstein, and C. Wu, *Physical Review letters* **80**, 145 (1998).
- [58] A. Holz, *Physical Review B* **22**, 3692 (1980).
- [59] L. Glasser and A. Every, *Journal of Physics A: Mathematical and General* **25**, 2473 (1992).
- [60] V. Bayot, E. Grivei, S. Melinte, M. Santos, and M. Shayegan, *Physical Review letters* **76**, 4584 (1996).
- [61] M. Rao, S. Sengupta, and R. Shankar, *Physical Review letters* **79**, 3998 (1997).
- [62] D. Hatch, T. Lookman, A. Saxena, and H. Stokes, *Physical Review B* **64**, 060104 (2001).
- [63] T. Shirahata, K. Shiratori, S. Kumeta, T. Kawamoto, T. Ishikawa, S.-y. Koshihara, Y. Nakano, H. Yamochi, Y. Misaki, and T. Mori, *Journal of the American Chemical Society* **134**, 13330 (2012).
- [64] X. Cheng, H. Gao, X. Tan, X. Yang, M. Prehm, H. Ebert, and C. Tschierske, *Chemical Science* **4**, 3317 (2013).
- [65] W. Qi, Y. Peng, Y. Han, R. K. Bowles, and M. Dijkstra, *Physical Review letters* **115**, 185701 (2015).
- [66] Y. Peng, F. Wang, Z. Wang, A. M. Alsayed, Z. Zhang, A. G. Yodh, and Y. Han, *Nature materials* **14**, 101 (2015).
- [67] Y. Peng, W. Li, F. Wang, T. Still, A. G. Yodh, and Y. Han, *Nature communications* **8**, 14978 (2017).
- [68] Y. Peng, W. Li, T. Still, A. G. Yodh, and Y. Han, *Nature Communications* **14**, 4905 (2023).
- [69] Y. Gao, *Materialia* **9**, 100588 (2020).
- [70] Y. Gao, Y. Wang, and Y. Zhang, *IUCrJ* **6**, 96 (2019).
- [71] C. Denoual and A. Vattré, *Journal of the Mechanics and Physics of Solids* **90**, 91 (2016).
- [72] R. Baggio, E. Arbib, P. Biscari, S. Conti, L. Truskinovsky, G. Zanzotto, and O. Salman, *Physical Review Letters* **123**, 205501 (2019).
- [73] R. Baggio, O. U. Salman, and L. Truskinovsky, *European Journal of Mechanics-A/Solids* **99**, 104897 (2023).
- [74] O. U. Salman, R. Baggio, B. Bacroix, G. Zanzotto, N. Gorbushin, and L. Truskinovsky, *Comptes Rendus. Physique* **22**, 201 (2021).
- [75] R. Baggio, O. Salman, and L. Truskinovsky, *Physical Review E* **107**, 025004 (2023).
- [76] N. Perchikov and L. Truskinovsky, *Journal of the Mechanics and Physics of Solids* **190**, 105704 (2024).
- [77] A. P. Thompson, H. M. Aktulga, R. Berger, D. S. Bolinteanu, W. M. Brown, P. S. Crozier, P. J. in't Veld, A. Kohlmeyer, S. G. Moore, T. D. Nguyen, *et al.*, *Computer Physics Communications* **271**, 108171 (2022).
- [78] LAMMPS software package, <http://lammms.sandia.gov>.
- [79] L. L. Boyer, *Phys. Rev. B* **53**, 3145 (1996).
- [80] See Supplemental Material at [URL-will-be-inserted-by-publisher] for the details of the simulations, deformation gradient, lattice invariant shears, configurational space, direct S→T transition, reverse T→S transition and grain misorientation. It also includes additional Refs.
- [81] P. F. Damasceno, L. G. V. Gonçalves, J. P. Rino, and M. Rita de Cássia, *Physical Review B* **79**, 104109 (2009).
- [82] K. Y. Lee and J. R. Ray, *Physical Review B* **39**, 565 (1989).
- [83] F. Shuang, P. Xiao, L. Xiong, and W. Gao, *Proceedings of the Royal Society A* **478**, 20220388 (2022).
- [84] P. Dorogokupets, A. Dymshits, K. Litasov, and

- T. Sokolova, Scientific reports **7**, 41863 (2017).
- [85] A. Dewaele, C. Denoual, S. Anzellini, F. Occelli, M. Mezouar, P. Cordier, S. Merkel, M. Véron, and E. Rausch, Physical Review B **91**, 174105 (2015).
- [86] H. Inoue, Y. Akahoshi, and S. Harada, Computational mechanics **16**, 217 (1995).
- [87] N. P. Kruyt and L. Rothenburg, J. Appl. Mech. **63**, 706 (1996).
- [88] S. Sengupta, P. Nielaba, M. Rao, and K. Binder, Physical Review E **61**, 1072 (2000).
- [89] P. H. Mott, A. S. Argon, and U. W. Suter, Journal of Computational Physics **101**, 140 (1992).
- [90] D. K. Ward, W. Curtin, and Y. Qi, Acta materialia **54**, 4441 (2006).
- [91] M. L. Falk and J. S. Langer, Physical Review E **57**, 7192 (1998).
- [92] M. Falk, Physical Review B **60**, 7062 (1999).
- [93] M. Horstemeyer and M. Baskes, MRS Online Proceedings Library (OPL) **578**, 15 (1999).
- [94] M. R. Mitchell, T. Tlusty, and S. Leibler, Proceedings of the National Academy of Sciences **113**, E5847 (2016).
- [95] P. Sartori and S. Leibler, bioRxiv , 2023 (2023).
- [96] J.-P. Eckmann, J. Rougemont, and T. Tlusty, Reviews of Modern Physics **91**, 031001 (2019).
- [97] J. A. Zimmerman, D. J. Bammann, and H. Gao, International Journal of Solids and Structures **46**, 238 (2009).
- [98] J. Ericksen, International Journal of Solids and Structures **6**, 951 (1970).
- [99] J. L. Ericksen, Advances in applied mechanics **17**, 189 (1977).
- [100] J. Ericksen, Arch. Rational Mech. Anal. **73**, 99 (1980).
- [101] L. Boyer, Acta Crystallographica Section A: Foundations of Crystallography **45**, fc29 (1989).
- [102] I. Folkins, Journal of mathematical physics **32**, 1965 (1991).
- [103] J. Wang, S. Yip, S. Phillpot, and D. Wolf, Physical Review letters **71**, 4182 (1993).
- [104] B. v. d. Waal, Acta Crystallographica Section A: Foundations of Crystallography **46**, fc17 (1990).
- [105] G. P. Parry, in *Mathematical Proceedings of the Cambridge Philosophical Society*, Vol. 80 (Cambridge University Press, 1976) pp. 189–211.
- [106] G. P. Parry, in *Mathematical Proceedings of the Cambridge Philosophical Society*, Vol. 82 (Cambridge University Press, 1977) pp. 165–175.
- [107] G. Parry, Archive for rational mechanics and analysis **145**, 1 (1998).
- [108] M. Pitteri, Journal of Elasticity **14**, 175 (1984).
- [109] M. Pitteri and G. Zanzotto, *Continuum models for phase transitions and twinning in crystals* (CRC Press, 2002).
- [110] E. Kaxiras and L. Boyer, Physical Review B **50**, 1535 (1994).
- [111] P. Engel, *Geometric crystallography: an axiomatic introduction to crystallography* (Springer Science & Business Media, 2012).
- [112] L. Michel, Physics Reports **341**, 265 (2001).
- [113] C. Thiel, J. Voss, R. J. Martin, and P. Neff, International Journal of Non-Linear Mechanics **112**, 57 (2019).
- [114] A. Stukowski, Modelling and simulation in materials science and engineering **18**, 015012 (2009).
- [115] V. Van Hoang and N. H. Giang, Physica E: Low-dimensional Systems and Nanostructures **113**, 35 (2019).
- [116] E. A. Jagla, Papers in physics **9**, 0 (2017).
- [117] M. Laguna and E. Jagla, Journal of Statistical Mechanics: Theory and Experiment **2009**, P09002 (2009).
- [118] M. F. Laguna, physica status solidi (b) **252**, 538 (2015).
- [119] M. Rechtsman, F. Stillinger, and S. Torquato, Phys. Rev. E **73**, 011406 (2006).
- [120] N. P. Kryuchkov, S. O. Yurchenko, Y. D. Fomin, E. N. Tsiok, and V. N. Ryzhov, Soft Matter **14**, 2152 (2018).
- [121] J. Ericksen, Mathematics and Mechanics of Solids **13**, 199 (2008).
- [122] P. Ming *et al.*, Archive for rational mechanics and analysis **183**, 241 (2007).
- [123] R. Béjaud, J. Durinck, and S. Brochard, Computational Materials Science **145**, 116 (2018).
- [124] Y. Gao, J.-H. Ke, B. Mao, Y. Liao, Y. Zheng, and L. K. Aagesen, Physical Review Materials **4**, 070601 (2020).
- [125] B. Dupé, B. Amadon, Y.-P. Pellegrini, and C. Denoual, Physical Review B **87**, 024103 (2013).
- [126] D. R. Trinkle III, *A theoretical study of the hcp to omega martensitic phase transition in titanium* (The Ohio State University, 2003).
- [127] D. Zahn and S. Leoni, Physical Review letters **92**, 250201 (2004).
- [128] S. Mahajan, M. Green, and D. Brasen, Metallurgical Transactions A **8**, 283 (1977).
- [129] J. Singh and S. Ranganathan, physica status solidi (a) **73**, 243 (1982).

Slip-dominated structural transitions: Supplemental Material

Kanka Ghosh,^{1,*} Oguz Umut Salman,¹ Sylvain Queyreau,¹ and Lev Truskinovsky^{2,†}

¹*CNRS, LSPM UPR 3407, Université Sorbonne Paris Nord, 93430 Villetaneuse, France*

²*PMMH, CNRS UMR 7636 ESPCI ParisTech, 10 Rue Vauquelin, 75005 Paris, France*

SIMULATION DETAILS

We model phase transition under hydrostatic pressure from a square lattice (S, plane space group p4mm) to a close-packed hexagonal lattice, interpreted here triangular lattice (T, plane space group p6mm).

MD simulations. We used Boyer potential presented in the main paper with $c_1 = c_2 = 2$ and $b_1 = b_2 = 8$ as in [1]. Then the choice $r_2/r_1=1.425$ (where r_2 and r_1 are second nearest neighbor distance and lattice parameter respectively) ensures that a square lattice with a lattice constant of 1.0659 Å is the ground state. We simulated 10^4 atoms with periodic boundary conditions (PBC) and used a cutoff distance $r_c = 2.5\text{Å}$. First the square crystal is equilibrated within NVT ensemble which takes 10^5 time steps with the step size $\Delta t = 0.0001$ ps. Then, the pressure control protocol is implemented within isothermal-isobaric (NPT) ensemble till the square phase is *marginalized*. A broad range of temperatures (10 K - 900 K) and pressures (0.1×10^7 bar - 2.4×10^7 bar) was considered to construct the T-P phase diagram presented in the main text. We used velocity Verlet algorithm and performed 10^7 MD steps (= 1 ns) to study the S-T transition at $T = 10$ K to avoid melting.

MS simulations. We used an athermal molecular statics protocol which implies that the effects of finite temperature were negligible. PBC were maintained throughout the simulation. Initially, a stable planar square crystal was prepared with 10^4 atoms using the same potential as in our MD simulations [1]. However, due to the fact that in athermal molecular statics thermodynamic pressure is an ambiguous concept and only virial pressure can be computed confidently, we had change the potential parameter r_2/r_1 from 1.425 to 1.3 to *marginalize* the square lattice while stabilizing triangular lattice. To induce the S-T transition we could then introduce a small disturbance by displacing all the atoms at random distances (about 0.9 % of the lattice parameter) along both x and y directions. The conjugate gradient algorithm was employed to conduct energy minimization.

Mesoscopic simulations. In our mesoscopic simulations we again used the same potential with square phase *marginalized* at the value of parameter $r_2/r_1 = 1.3$. Within the framework of our mesoscopic tensorial model (MTM), the globally periodic Landau potential $\phi(\mathbf{C})$ was

constructed using the Cauchy-Born rule from the same interatomic potential as in our MD and MS numerical experiments [1].

The energy was extended by symmetry beyond the minimal periodicity domain. It implies the representation of an arbitrary metric tensor \mathbf{C} in the form $\tilde{\mathbf{C}} = \mathbf{m}^T \mathbf{C} \mathbf{m}$ where \mathbf{m} is a unimodular integer-valued matrix and $\tilde{\mathbf{C}}$ is an image of \mathbf{C} inside the minimal periodicity domain in the sense that $\phi(\tilde{\mathbf{C}}) = \phi(\mathbf{C})$.

In Figure S1 we illustrate the \mathbf{C} -space (Poincaré disk, see the detailed explanations below) with the superimposed computed strain energy landscape for three values of the parameter r_2/r_1 as it gradually changes from 1.425 to 1.3. One can see that the energy minima (indicated via dark blue) eventually shift from square configuration (see ‘S’ in Fig. S1(a)) to triangular configuration (see equivalent triangular minima ‘T₁’ and ‘T₂’ in Fig. S1(c)).

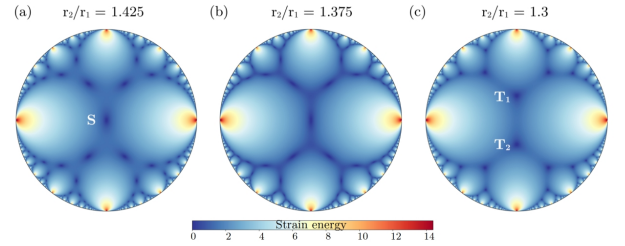


FIG. S1: Strain energy landscape (color coded) in the configurational \mathbf{C} -space (Poincaré disk) at three different values of the Boyer parameter r_2/r_1 . Letters indicate the square (S) and the two relevant triangular minima (T₁, T₂). The colors represent the strain energy level.

We associated the elastic energy $\phi(\mathbf{C})$ with the node \mathbf{x} assuming that $\mathbf{C} = \nabla \mathbf{y}^T \nabla \mathbf{y}$. The piecewise linear deformation field $\mathbf{y}(\mathbf{x})$ was discretized using shape functions as described in the main text which turned the problem into finite dimensional, parameterized by displacements of the 2D network of discrete nodes identified by their integer-valued coordinates ij . Parametric minimization of the discretized energy functional $W = \int_{\Omega_0} \phi d\Omega_0$ was accomplished using a variant of conjugate gradient optimization known as the L-BFGS algorithm [2]. This algorithm seeks solutions to the equilibrium equations $\partial W / \partial \mathbf{u}_{ij} = \int_{\Omega_0} \mathbf{P} \nabla \mathcal{N}_{ij} d\Omega_0 = 0$, where $\mathbf{P} = \partial \phi / \partial \nabla \mathbf{y}$, \mathbf{u}_{ij} denote the values of displacement at node ij , \mathcal{N}_{ij} is the shape function at node ij and Ω_0 is defined as the computational domain. In our numerical experiments we used (discretized) free boundary conditions $\mathbf{P} \cdot \mathbf{N} = 0$,

where \mathbf{N} is the normal to the surface at the reference state. The S-T transformation was again initiated by incrementally changing the potential parameter r_2/r_1 from the value 1.425 to the value 1.3. This ensured the eventual shift in the nature of the ground state configuration from square to triangular.

DEFORMATION GRADIENT

In Figure S2, we show the mapping which schematically describes the deformation of an atomic neighborhood.

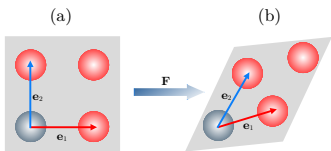


FIG. S2: The schematic description of the deformation of the chosen ‘atomic neighborhood’; (a), (b) show the reference and the deformed states, respectively.

Suppose that in a two-dimensional lattice a reference point is represented by a vector $\mathbf{X} = \{X_1, X_2\}$ while its deformed position is represented by the vector $\mathbf{x} = \{x_1, x_2\}$. Then, the deformation gradient is $F_{iI} = \partial x_i / \partial X_I$, where the indexes i, I refer to deformed and reference coordinate systems, respectively. If $\mathbf{R}^{\alpha\beta}$ and $\mathbf{r}^{\alpha\beta}$ are the vectors connecting atom α with its neighbors (β or $\beta_1, \beta_2, \dots, \beta_n$ for n neighbors) in the reference and in the actual configurations respectively, the approximate deformation gradient obtained by minimizing mean-square difference between the actual displacements of the neighboring atoms relative to the chosen central atom and the relative displacements, that they would have had if they were in a region of uniform strain, can be written as $F_{iI}^\alpha = \omega_{iM}^\alpha (\eta_{IM}^\alpha)^{-1}$, where $\omega_{iM}^\alpha \equiv \sum_{\beta=1}^n r_i^{\alpha\beta} R_M^{\alpha\beta}$ and $\eta_{IM}^\alpha \equiv \sum_{\beta=1}^n R_I^{\alpha\beta} R_M^{\alpha\beta}$ [3]. As a representative atomic neighborhood we found sufficient to choose two non collinear nearest neighbors and one of the second nearest neighbors as the averaging domain, see Fig. S2. In other words, the chosen atomic neighborhood of a particle is made of two complementary triangular domains. Atomistic strain tensor \mathbf{C} is recovered from the deformation gradient via the formula $\mathbf{C} = \mathbf{F}^T \mathbf{F}$.

LATTICE INVARIANT SHEARS

Lattice invariant shear is a crystallographically specific affine volume preserving deformation which transforms an infinite lattice into itself. General lattice invariant shears are described by the deformation gradients

represented by the integer valued unimodular matrices $\{\mathbf{m}, m_{IJ} \in \mathbb{Z}, \det(\mathbf{m}) = 1\}$, see [4, 5] for the details.

For instance, consider a square lattice (S) which is homogeneously deformed with the deformation gradient given by the formula $\mathbf{F}(\alpha) = \mathbb{1} + \alpha \mathbf{e}_1 \otimes \mathbf{e}_2$, where α denotes the amplitude of shear, $\mathbf{e}_1, \mathbf{e}_2$ represent unit base vectors along x and y directions, respectively. Such deformation describes one parametric family of simple shears.

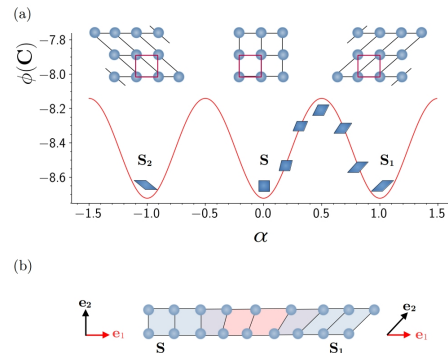


FIG. S3: (a) Schematic representation of the strain energy $\phi(\mathbf{C})$ as a function of a simple shear amplitude α (see the text). The insets schematically depict the equivalent square lattice configurations S_2, S and S_1 . (b) Schematic presentation of an edge dislocation.

Our Fig. S3(a) presents schematic structure of the strain energy landscape $\phi(\mathbf{C})$ as a function of shear amplitude α . As one increases the parameter α from zero, which corresponds to a minimum of the energy, the function $\phi(\alpha)$ first reaches its maximum but then decreases reaching again a symmetry related minimum at $\alpha = 1$. At this point an equivalent lattice is obtained. Similarly, negative increment of α transforms at $\alpha = -1$ the original lattice configuration into yet another symmetric configuration with exactly the same energy. The insets of Fig. S3(a) schematically describe three equivalent lattice configuration S, S_1 and S_2 corresponding to three equivalent energy minima. Note that if we remove the bonds in those insets and leave only atoms, the corresponding three atomic configurations will be indistinguishable. Furthermore, our Fig. S3(b) presents a schematic structure of an edge dislocation which can be viewed as a ‘domain wall’ between a sheared (S_1 in this case) and undeformed (S) ‘phases’.

An image of the same edge dislocation in the Poincaré disk (see the definition below) with the superimposed $GL(2, \mathbb{Z})$ invariant energy landscape is shown in Fig. S4. Here our simple shear parametrized by α is represented by a curve which contains equivalent square lattices S, S_1 and S_2 related via ‘lattice invariant simple shears’. Similarly, the equivalent triangular lattices T_1 and T_2 are related via two symmetric ‘lattice invariant simple shears’ only one of which is shown in Fig. S4(b).

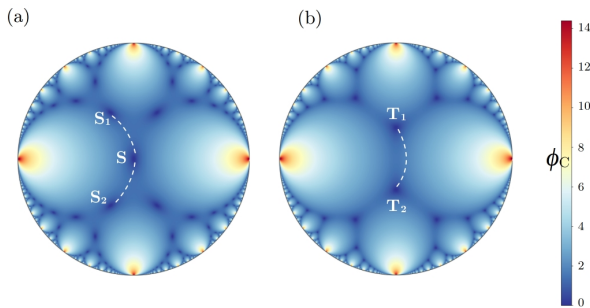


FIG. S4: (a) Schematic presentation of an edge dislocation linking equivalent square lattices on a Poincaré disk. (b) Similar edge dislocation in the case of triangular lattice. Dashed lines represent examples of lattice invariant simple shear paths. The colors represent the strain energy level.

CONFIGURATIONAL SPACE

The 3D space of symmetric metric tensors with coordinates (C_{11}, C_{22}, C_{12}) contains a subspace describing isochoric deformations and selected by the condition $C_{11}C_{22} - C_{12}^2 = 1$. This is our 2D configurational space. The action of the infinite discrete symmetry group $GL(2, \mathbb{Z})$ naturally tessellates the configurational space into periodicity domains. A convenient approach to visualize globally the subspace of metric tensors \mathbf{C} with $\det(\mathbf{C}) = 1$ is to use a stereographic projection of the corresponding hyperbolic surface in the (C_{11}, C_{22}, C_{12}) space onto a unit disk, which is known as the Poincaré disk, see Fig. S5.

The geometrically minimal periodicity domain in the configurational space, known as the *fundamental* domain is $\mathcal{D} = \{2C_{12} \leq \min(C_{11}, C_{22})\}$, see for instance a dark gray triangular area in Fig. 3(a) in the main text; it corresponds to the ‘minimal’ choice for the lattice vectors $\tilde{\mathbf{e}}_1, \tilde{\mathbf{e}}_2$, selected by the Lagrange reduction algorithm [6–13]. The three boundaries of the fundamental domain \mathcal{D} can be presented explicitly in the parametric form:

$$\mathbf{C} = \begin{pmatrix} \alpha^2 & 0 \\ 0 & \frac{1}{\alpha^2} \end{pmatrix}, 0 < \alpha \leq 1, \quad (1)$$

$$\mathbf{C} = \begin{pmatrix} \alpha^2/4 + 1/\alpha^2 & -\alpha^2/4 + 1/\alpha^2 \\ -\alpha^2/4 + 1/\alpha^2 & \alpha^2/4 + 1/\alpha^2 \end{pmatrix}, 0 < \alpha \leq \sqrt{2} \quad (2)$$

and

$$\mathbf{C} = \begin{pmatrix} \alpha^2 & \alpha^2/2 \\ \alpha^2/2 & \alpha^2/4 + 1/\alpha^2 \end{pmatrix}, 0 < \alpha \leq \gamma. \quad (3)$$

The $GL(2, \mathbb{Z})$ copies (replicas) of these boundaries, constitute the tessellation of the configurational space, represented in Fig. S5 by the thin black lines which are divided (artificially) into solid and dashed ones for easier identification. To construct such copies one needs

to apply to (1-3) the group action $\tilde{\mathbf{C}} = \mathbf{m}^T \mathbf{C} \mathbf{m}$, where $\{\mathbf{m}, m_{IJ} \in \mathbb{Z}, \det(\mathbf{m}) = \pm 1\}$.

The *elastic domain*, which would describe fully the elastic response of a single-well material as well as the behavior of a solid undergoing Landau type structural phase transition, is also known in the literature as the maximal Ericksen-Pitteri neighborhood [6, 10, 11]. It can be obtained from \mathcal{D} by applying discrete transformations forming the crystallographic point group $P(\mathbf{e}_I)$, which contains only rigid rotations and is used to characterize material symmetries within classical continuum elasticity [6, 11].

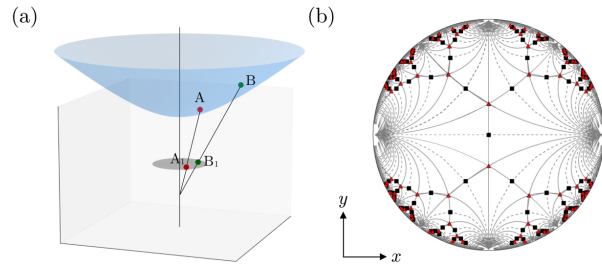


FIG. S5: (a) Three dimensional hyperbolic surface $C_{11}C_{22} - C_{12}^2 = 1$ in the configurational space of metric tensors C_{11}, C_{22}, C_{12} projected onto a Poincaré disk: the points A, B on such a surface are mapped to the points A_1, B_1 on the disk. (b) Poincaré disk: thin lines indicate the boundaries of minimal periodicity domains; points on the disk describing equivalent square and triangular lattices are marked by black squares and red triangles, respectively.

In the main paper we presented a structure of the $GL(2, \mathbb{Z})$ tessellation of the Poincaré disk in the two cases: when the reference state corresponds to a square lattice S or to a triangular lattice T_1 .

To obtain such a representation in the case when the reference state is a square lattice, we first define the corresponding reference basis $\mathbf{e}_1 = \{1, 0\}, \mathbf{e}_2 = \{0, 1\}$. The deformed basis is then $\mathbf{f}_i = \mathbf{F}\mathbf{e}_i$, where $i = 1, 2$ and \mathbf{F} is the deformation gradient. Under the assumption that $\det \mathbf{F} = 1$ we can introduce metric tensors $\mathbf{C} = \mathbf{F}^T \mathbf{F}$ describing different states in our configurational space. These metric tensors are then projected onto the Poincaré disk using the rectangular coordinates on the disk: $x = t(C_{11} - C_{22})/2, y = tC_{12}$, where $t = 2(2 + C_{11} + C_{22})^{-1}$, see Fig. S5.

To obtain a similar representation in the case when the reference state is a triangular lattice, we first write the basis vectors of the triangular lattice T_1 in the coordinates of the basis of the square lattice S: $\mathbf{h}_1 = \{\gamma, 0\}$ and $\mathbf{h}_2 = \{\gamma/2, \gamma\sqrt{3}/2\}$, where $\gamma = (4/3)^{1/4}$. We then introduce a matrix \mathbf{H} whose columns are the vectors $\mathbf{h}_{1,2}$. Since $\mathbf{h}_j = \mathbf{H}\mathbf{e}_i$ the metric tensor in this new (triangular lattice) basis takes the form $\mathbf{C}' = \mathbf{H}^{-T} \mathbf{C} \mathbf{H}^{-1}$ where \mathbf{C} is the metric tensor in the old (square lattice) basis. Now the components of the tensor \mathbf{C}' can be stereographically

projected into the Poincaré disk using the same mapping as before which gives rise to a tessellation presented in Fig. 3(b) in the main text. While in both cases the *fundamental domains* \mathcal{D} have the same triangular shape, the *elastic domains* are different as the point group involves four rotations when the reference lattice is square and six rotations when it is triangular, see the light gray areas in Fig. 3(a,b) in the main text.

DIRECT TRANSITION S \rightarrow T

Molecular dynamics. We begin with highlighting that our Fig. 2 and Fig. 5 in the main text represent the outcome of the same MD numerical experiment, see their direct juxtaposition in Fig. S6. Both figures show the same transformed triangular crystal with the only difference is that in Fig. 2 atoms are colored according to their potential energies per atom, see the reproduction in Fig. S6(a), whereas in Fig. 5, which we present now as two separate figures Fig. S6 (b,c), atoms inside two different triangular phase grains are colored according to the value of the particular components of the deformation gradient: F_{12} in Fig. S6(b) and F_{21} in Fig. S6(c). More specifically, the fragment A in Fig. S6(a) is shown in Fig. S6(b) emphasizing the component F_{12} because it presents an example of a horizontal micro-layering (crystallographically specific finite shuffling). Instead, the fragment B in Fig. S6(a) is represented in Fig. S6(c) emphasizing the component F_{21} as the micro-layering in this case is vertical. Note that the selective coloring of the grains in Fig. S6(b,c) is chosen for convenience, in particular the gray areas there do not indicate the presence of the square phase which has completely disappeared in the shown product (triangular) phase: the gray areas in Fig. S6(b,c) indicate instead that either $F_{12}=0$ or $F_{21}=0$ in the corresponding regions.

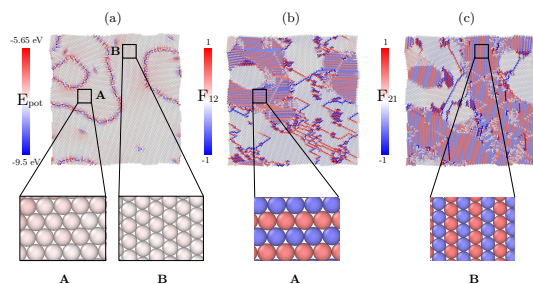


FIG. S6: Transformed triangular polycrystal in MD numerical experiment with atoms colored using: (a) potential energies per atom, (b) F_{12} and (c) F_{21} . Two fragments A and B are also shown as insets.

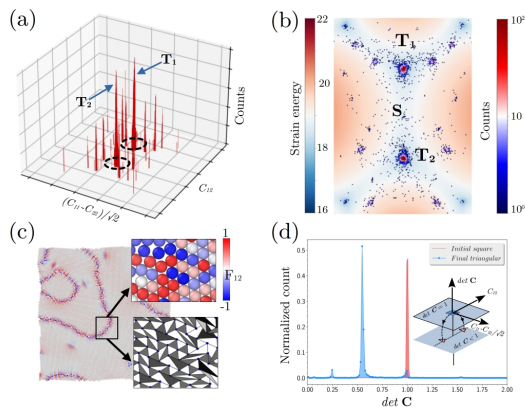


FIG. S7: The S-T transition in the \mathbf{C} -space. (a) 3D histogram representation of the strain distribution in triangular phase; note that the ‘counts’ axis has a logarithmic scale. (b) 2D histogram representation of the same strain distributions shown against the corresponding energy landscape. (c) A highly deformed atomic fragment around the grain boundary; both deformation gradient distribution and the deformed triangulation network are shown in the two insets. (d) The distribution of $\det \mathbf{C}$ in the initial square (red) and the final triangular lattices (blue).

In MD simulations the distribution of the values of \mathbf{C} over the atoms representing individual neighborhoods evolves during the S-T transition. The transformation starts when the values of \mathbf{C} in all nodes are the same which means that the distribution is fully localized at the origin representing unstressed square lattice S. At the end of the transformation when the T phase is nominally reached, the configurational points spread in the \mathbf{C} -space.

Our Fig. S7 illustrates the final strain distribution projected on $\det \mathbf{C} = 1$ surface. The three dimensional histogram representation of the strain distribution, see Fig. S7(a), indicates that most of the elements are in either T_1 or T_2 energy wells. This is also seen in 2D histogram of the same atomistic strains shown in the Fig. S7(b). Note however, that in addition to the most populated T_1 and T_2 triangular configurations, several other locations outside the T_1 and T_2 energy wells within the \mathbf{C} -space are also occupied. Some of them correspond to grain boundaries like the one in the fragment shown in Fig. S7(c). In Fig. S7(d) we illustrate the fact that the S-T transformation is accompanied by a volumetric contraction. Specifically, the original S phase with $\det \mathbf{C} = 1$ transforms into the final T phase with $\det \mathbf{C} = 0.55$.

Molecular statics. Simulations of S-T transition using athermal molecular statics (MS) exhibited all the main ingredients of the transformation mechanism observed in MD experiments. In particular, our Fig. S8(a–h) shows that the lattice scale alternate plastic slips involving both, atomic rows and atomic columns, are recovered. Thus, we observe in neighboring grains the same alternating mixtures of configurations T_1^+ , T_2^- (realized via alternating F_{12}^\pm) and of configurations T_1^- , T_2^+ (realized

via alternating F_{21}^{\pm} , see Fig. S8(g,h). The evolution of the strain populations inside the \mathbf{C} -space indicates the same mechanism involving concurrent symmetric pure shears. Specifically, our Fig. S8(i-k) shows that the atomic strains spread via rhombic valleys towards the triangular energy minima T_1 and T_2 .

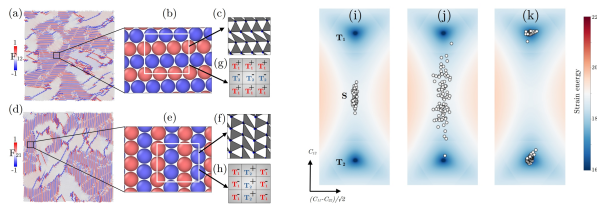


FIG. S8: (a), (d) The distribution of deformation gradient components F_{12} and F_{21} in the transformed triangular phase obtained in MS simulations. (i)–(k) Evolution of the atomistic strain distribution in the \mathbf{C} -space.

A minor difference is that in our MS experiments the S-T transformation proceeded in almost isochoric conditions. Indeed, due to lack of thermodynamic control parameters in the athermal MS protocol, we had to induce the S-T transition by changing the potential parameter r_2/r_1 from 1.425 to 1.3. To capture the structural transformation, radial distribution function $g(r) = \frac{1}{\pi r^2 N \rho} \sum_{i=1}^N \sum_{j \neq i}^N \langle \delta(\mathbf{r} - |\mathbf{r}_j - \mathbf{r}_i|) \rangle$ is calculated for our 2D crystal, where $\rho = N/A$ is the density, N is the total number of atoms and A is the area of the system. The distance between the atoms i and j is represented by the difference $\mathbf{r}_j - \mathbf{r}_i$. As a result of the athermal S-T transition, the lattice constant changed from 1.0659 Å (r_0 in Fig. S9(a)) in the ‘S’ phase to 1.14 Å (r_{eq} in Fig. S9(b)) in the ‘T’ phase, see Fig. S9(a), (b). The corresponding areas for the square unit cell is $r_0^2 = 1.1361$ Å² and for the triangular lattice (rhombic cell) is $\frac{\sqrt{3}}{2} r_{eq}^2 = 1.125$ Å². The ratio of the unit cells is then $\frac{area_{\square}}{area_{\Delta}} = 1.009$. Therefore, the unit cell areas of the initial ‘S’ phase and the transformed ‘T’ phase are almost identical in MS numerical experiments.

However, it is known that the S-T transition must necessarily come with the increase of the packing fraction as, for instance, triangular/hexagonal lattice is closed-packed while its square counterpart is not. Specifically, the packing fraction, defined as the ratio of the area occupied by the circles inside the unit cell and that of the area of the unit cell, in ‘S’ phase is $\frac{\pi a^2}{4}/a^2 = \frac{\pi}{4} \approx 0.785$ while in ‘T’ phase it is $\frac{1}{2}\pi \frac{a^2}{4}/\frac{\sqrt{3}a^2}{4} = \frac{\pi}{2\sqrt{3}} \approx 0.907$, see the distribution of the coordination numbers n_c in Figure S9(c).

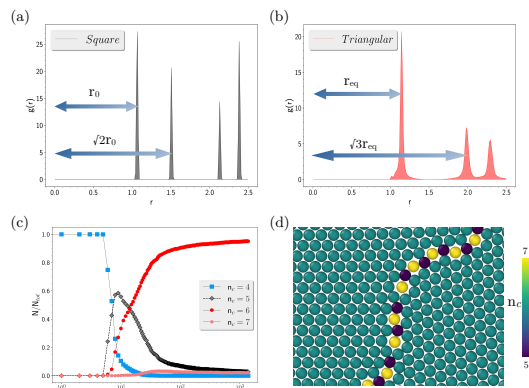


FIG. S9: Radial distribution functions $g(r)$ for the initial square lattice (a) and for the transformed triangular crystal (b). In (c) we show the variation during the S-T transition of the fractions of atoms (N/N_{tot}) characterized by different coordination (n_c). A fragment of the misoriented triangular grains with atoms colored according to their coordination is shown in (d).

Therefore, in view of the similarities of the parameters of the unit cells, the S-T transition should result in the formation of ‘void space’ that is realized through the formation of less dense grain boundaries, see the fragment shown in Fig. S9(d). In particular, we see that the atoms constituting grain boundaries with $n_c = 5, 7$ are differently coordinated vis a vis atoms inside the triangular grains where $n_c = 6$. Our numerical experiments show that around 5 % of atoms constitute effectively loose grain boundaries against 95 % of atoms inside the close packed grains.

Mesoscopic tensorial model. The finite element simulation of the S-T transition started again with a finite element configuration describing a marginally stable phase S. The mechanism of the transformation into a T phase followed closely what we have already seen in our MD and MS simulations. For example, in Fig. S10 we show two snapshots of the distribution of MTM strains in \mathbf{C} -space. Similar to what we have seen in our atomistic

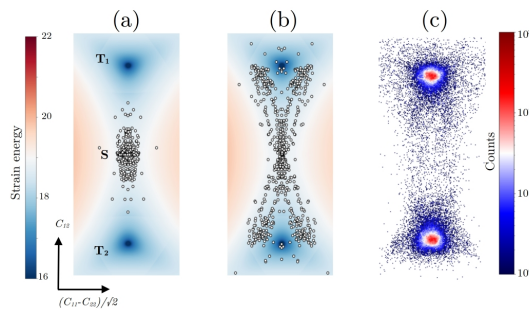


FIG. S10: S-T transformation in MTM numerical experiments: (a,b) fragments of the \mathbf{C} -space illustrating two successive stages of S-T transition; (c) the histogram showing the distribution of the values of \mathbf{C} in the final state.

simulations, the transformed triangular lattice evolves as a mixture of two triangular configurations T_1 and T_2 . Thus, we again observed alternating layer-wise propagation (both horizontal and vertical) of triangular phase. These results show that within the coarse-grained description the front-propagation-based mechanism of S-T reconstructive transition producing micro-plastically deformed triangular phase is preserved.

REVERSE TRANSITION T→S

Even though in much less detail, we have also performed numerical experiments involving the reverse transition from triangular to square phase. More specifically, we performed cyclic loading producing a hysteresis loop and exhibiting a succession of two S→T→S reconstructive transitions.

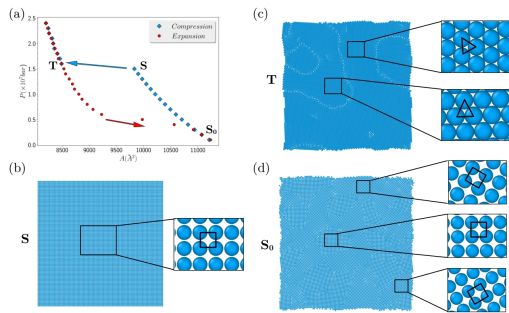


FIG. S11: S→T→S reconstructive transition in preliminary MD simulations. (a) P-V(area A) phase diagram of the complete compression-expansion cycle. With the letters S, T, and S_0 we denote : pristine square, transformed triangular lattice under compression and transformed square lattice after the subsequent expansion. Insets in (b), (c), and (d) show microscopic configurations with their associated multi-grain compositions.

In Fig. S11(a) we illustrate the hysteretic nature of the square to triangular transition in MD by showing the complete compression-expansion cycle on the P-V (area A) plane. Specifically, as in our main discussion, we start with a defect-free (pristine) 2D square crystal, see Fig. S11(b), and employ isotropic compression (by increasing hydrostatic pressure) to induce the transformation into a triangular phase. The resulting configuration of misoriented triangular grains, see Fig. S11(c), is then subjected to isotropic expansion via the reduction of pressure. This brings the system back into the square phase which is now also represented by a texture of misoriented square grains, see Fig. S11(d). The insets reveal that as a result of the S→T→S cycle the original highly symmetric ‘cold’ square phase S develops into a multi-grain ‘hot’ configuration S_0 which is obviously more generic and entropically favored.

To corroborate these results, we also performed slightly

different athermal MS numerical experiments, see Fig. S12. Here we studied the transition from a pristine triangular phase to a multi-grain square phase by changing the value of parameter r_2/r_1 from 1.3 to 1.425. As we have already mentioned, this modifies the ground state of the lattice from triangular to the square symmetry. The resulting grain texture exhibits the same misorientation angles as in our MD simulation and also reveals a hidden alternating slip distribution behind the apparent homogeneous rotations of the product phase (not shown here). A systematic study of the S-T transition including the comparison with the results of the MTM simulations is underway and the discussion of the detailed structure of the resulting hysteretic cycle is left for a separate study.

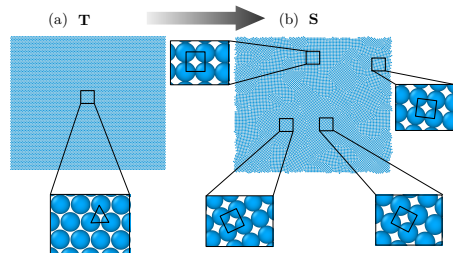


FIG. S12: Preliminary modeling of T→S transition using athermal MS simulations: (a) pristine triangular lattice (T), (b) transformed square (S) lattice represented by a texture of misoriented grains. Fragments of ‘T’ and ‘S’ grains with their associated orientations are shown in the insets.

GRAIN MISORIENTATION

Here we clarify how the misorientation between the grains was quantified in the main text. We focus then on the direct S-T transition and deal with the grain structure inside the product triangular (hexagonal) phase. Note first that the reference orientation of the triangular basis is chosen in such a way that e_1 is horizontal and e_2 forms with it a 60° angle, see Fig. S13. The misorientation angle characterizes the rotation which relates the basis vectors in two neighboring grains. Our Fig. S13(a) shows a fragment of the product triangular lattice featuring two grains separated by a grain boundary and it is clear from this figure that the basis vectors in the left grain need a 30° rotation to transform into the basis vectors on the right.

However, as we explain in the main text, the same misorientation angle can also be computed analytically. For instance, we show below how one can evaluate the relative rotation of the T_1^+ and T_1^- components of the microtwin patterns representing two neighboring triangular grains shown in Fig. S13.

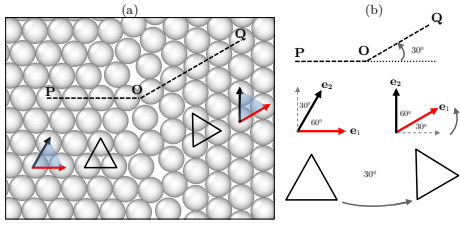


FIG. S13: (a) A fragment of the product polycrystalline triangular phase showing two misoriented grains separated by a grain boundary; (b) basis vector \mathbf{e}_1 and \mathbf{e}_2 in both grains. The identification of elementary cells in (b) shows that they are related via a 30° rotation.

Recall that the coexisting variants T_1^+ and T_1^- are obtained from the S phase via deformation gradients $\mathbf{F}_1^\pm = \mathbf{R}_1^\pm \mathbf{U}_1$, where

$$\mathbf{U}_1 = \frac{1}{2} \begin{bmatrix} \lambda_* + \frac{1}{\lambda_*} & \lambda_* - \frac{1}{\lambda_*} \\ \lambda_* - \frac{1}{\lambda_*} & \lambda_* + \frac{1}{\lambda_*} \end{bmatrix}, \quad (4)$$

with $\lambda_* = 3^{1/4}$ and

$$\mathbf{R}_1^\pm = \frac{1}{\sqrt{\cosh \alpha}} \begin{bmatrix} \cosh(\alpha/2) & \pm \sinh(\alpha/2) \\ \mp \sinh(\alpha/2) & \cosh(\alpha/2) \end{bmatrix}, \quad (5)$$

with $\alpha = 2 \ln(\lambda_*)$. The corresponding rotation angles are ϑ_\pm where

$$\vartheta_\pm = \sin^{-1} \left[\pm \frac{\sinh(\alpha/2)}{\sqrt{\cosh(\alpha)}} \right] \frac{180^\circ}{\pi} = \pm 15^\circ, \quad (6)$$

where clockwise and counter clockwise rotations are denoted via ‘+’ and ‘-’ respectively, see Fig. S13 (b). Note that the rotations $\mathbf{R}_1^+(\vartheta)$ and $\mathbf{R}_1^-(\vartheta)$ align the basis vectors \mathbf{e}_1 and \mathbf{e}_2 of the T_1 lattice with the horizontal and vertical directions, respectively. Therefore, the misorientation between the variants T_1^+ and T_1^- is exactly 30° as we have already seen in Fig. S13 (a).

Similarly, analysis for the coexisting variants T_2^+ and T_2^- shows that the misorientation between them is again 30° , see for instance Fig. 4(b) in the main text. We reiterate that similar to variants T_1^+ and T_1^- , the variants T_2^+ and T_2^- reside in neighboring grains separated by the same grain boundary.

* kanka.ghosh@lspm.cnrs.fr

† lev.truskinovsky@espci.fr

- [1] L. L. Boyer, Phys. Rev. B **53**, 3145 (1996).
- [2] S. Bochkhanov and V. Bystritsky, Available from: <https://www.alglib.net> (2013).
- [3] J. A. Zimmerman, D. J. Bammann, and H. Gao, International Journal of Solids and Structures **46**, 238 (2009).
- [4] R. Baggio, E. Arbib, P. Biscari, S. Conti, L. Truskinovsky, G. Zanzotto, and O. Salman, Physical Review Letters **123**, 205501 (2019).
- [5] O. U. Salman, R. Baggio, B. Bacroix, G. Zanzotto, N. Gorbushin, and L. Truskinovsky, Comptes Rendus. Physique **22**, 201 (2021).
- [6] S. Conti and G. Zanzotto, Archive for rational mechanics and analysis **173**, 69 (2004).
- [7] G. P. Parry, in *Mathematical Proceedings of the Cambridge Philosophical Society*, Vol. 80 (Cambridge University Press, 1976) pp. 189–211.
- [8] G. P. Parry, in *Mathematical Proceedings of the Cambridge Philosophical Society*, Vol. 82 (Cambridge University Press, 1977) pp. 165–175.
- [9] G. Parry, Archive for rational mechanics and analysis **145**, 1 (1998).
- [10] M. Pitteri, Journal of Elasticity **14**, 175 (1984).
- [11] M. Pitteri and G. Zanzotto, *Continuum models for phase transitions and twinning in crystals* (CRC Press, 2002).
- [12] P. Engel, *Geometric crystallography: an axiomatic introduction to crystallography* (Springer Science & Business Media, 2012).
- [13] L. Michel, Physics Reports **341**, 265 (2001).